Chemical Science

ROYAL SOCIETY OF CHEMISTRY

EDGE ARTICLE

View Article Online
View Journal

Cite this: DOI: 10.1039/d6sc02038k

All publication charges for this article have been paid for by the Royal Society of Chemistry

NH_4^+-mediated interfacial chemistry for collaborative dual-pathway high-mass-loading energy storage

Jinxin Wang,† Wei Guo,†* Mingming Sun, Geng Zhang, Mengting Cheng, Wenbin Xie, Na Hu, Yuehan Yang and Qiuyu Zhang *

The deposition/dissolution mechanism of MnO_2 with two-electron transfer is promising for high-energy aqueous energy storage. However, this reaction is severely limited by the kinetically unfavorable dissolution step, a challenge that is greatly exacerbated as the deposit thickens. Herein, by refining NH_4^+-mediated interface chemistry, we achieve the precise configuration of MnO_2 with controlled hydroxylation, which guides the reversible MnO_2/Mn^{2+} conversion under high-mass-loading conditions. The partially hydroxylated surface further creates a kinetically favorable microenvironment for NH_4^+ storage, ultimately leading to energetic dual-pathway storage behaviors. This enables a remarkable areal capacitance of 13.8 F cm^{-2} and sound cycling stability over 6000 cycles under high-mass-loading conditions (27.1 mg cm^{-2}). Theoretical calculations reveal that the controlled partial hydroxylation of MnO_2 promotes electronic conduction and lowers the adsorption energy of NH_4^+, outperforming both highly hydroxylated and pure MnO_2. The adsorbed NH_4^+ delivers intimate interfacial electronic interaction with partially hydroxylated MnO_2 to trigger local charge redistribution, substantially lowering the MnO_2/Mn^{2+} conversion energy barrier of the nonspontaneous rate-determining step at the NH_4^+-proximal site. Our findings highlight the significance of the interfacial microenvironment governing the collaborative dual-pathway storage chemistry, which provides guidance for boosting high-mass-loading energy storage.

Received 11th March 2026
Accepted 6th April 2026

DOI: 10.1039/d6sc02038k

rsc.li/chemical-science

Introduction

The escalating global energy crisis and climate change highlight the great demand for developing clean and sustainable energy techniques,[1–3] *e.g.*, aqueous electrochemical energy storage with inherent safety, environmental friendliness, and cost-effectiveness.[4,5] MnO_2 has been widely considered as an economic and highly promising cathode alternative in a near-neutral environment, featuring a wide operating voltage and high theoretical capacitance.[6,7] However, the sluggish kinetics and the poor stability occur under commercial-level mass loading (≥10 mg cm^{-2}), posing significant challenges for sustaining efficient practical applications of MnO_2 electrodes so far.[8,9]

Tremendous efforts have been made to tailor the reactivity and kinetics behaviors of the electrode materials by controlling the microstructure and local reaction environment toward optimal carrier-intercalation/diffusion and interface behaviors.[7,9–13] For instance, it was reported that the structural stability issue can be partially relieved by harnessing the physical confinement effect and abundant interfacial interactions.[13,14] In another case, robust electronic coupling between the heteroatom and the Mn atom was developed to suppress the structure deformation and Jahn–Teller effect during cycling.[15,16] Despite the progress, under practical scenarios with substantially increased electrode thickness and non-active substances, significant kinetics limitations still exist to compromise the storage capability, stemming from the super-long diffusion distance and complicated interfacial redox process.[17–19] Beyond that, the dynamic reconstruction of the surface/interface happens with deactivation and dissolution, creating a varied local reaction microenvironment over time that requires better control.

In contrast to intercalation chemistry, the MnO_2/Mn^{2+} deposition/dissolution chemistry provides a new opportunity for highly efficient energy storage. The *in situ* formation and interface reset during the charge/discharge process can bypass the undesired compositional/structural evolution and considerable local strain accumulation, responsible for breaking the limitations for energetic and sustainable high-mass-loading applications. Moreover, the topological structure and the spatial arrangement of MnO_2 can be tailored by refining the cation environment and the reactivity. For better practice, the

School of Chemistry and Chemical Engineering, Key Laboratory of Special Functional and Smart Polymer Materials of Ministry of Industry and Information Technology, Northwestern Polytechnical University, Xian 710072, China. E-mail: weiguo-nwpu@nwpu.edu.cn; qyzhang@nwpu.edu.cn

† These authors contributed equally to this work.

high concentration of Mn^{2+} is preferred to boost the deposition behaviors and thereby the charges stored. However, a high-concentration pure Mn^{2+} electrolyte leads to the suppressed dissolution of MnO_2 according to Le Chatelier's principle. At the same time, the deposited thick MnO_2 features highly compromised mass/charge-transfer rates with an inferior utilization rate of active species. An open question appears regarding how to enable better control of the deposition/dissolution chemistry with enhanced conversion kinetics under high Mn^{2+} concentration conditions. Besides, it is predicted that synergistically coupling the cation storage with the MnO_2/Mn^{2+} conversion chemistry may potentially boost high-mass-loading energy storage with ultra-efficient utilization of active species. The mechanistic insights can help the step-forward optimization of high-mass-loading energy storage techniques for better applications.

Herein, by introducing NH_4^+ into a dynamic environment, we overcome the kinetics limitation of MnO_2/Mn^{2+} conversion and trigger its synergistic coupling with NH_4^+ (de)intercalation chemistry toward an optimal integrated reaction system. This dual-pathway storage mechanism enables a high areal capacitance of 13.8 F cm^{-2} for electrodes with a superhigh mass loading of 27.1 mg cm^{-2}, along with a good capacitance retention of 80% after 6000 cycles. The theoretical and experimental results indicate that NH_4^+ acts as the modulator at the reaction interface to precisely control the hydroxylation degree of MnO_2, creating a kinetically favorable reaction microenvironment with fast electronic conduction and enhanced interfacial NH_4^+ adsorption. Furthermore, the adsorption of NH_4^+ on the reconstructed interface triggers a local charge redistribution, which substantially reduces the energy barrier of the nonspontaneous rate-determining step during dissolution of MnO_2, thereby promoting an energetic dual-pathway storage mechanism. This work offers novel insights into cationic environment engineering for mutual manipulation of deposition/dissolution and intercalation chemistry, and provides a promising avenue for tailoring better high-mass-loading energy storage.

Results

Refining the interfacial microenvironment for favoring MnO_2/Mn^{2+} conversion

Our previous study has demonstrated that dissolved Mn^{x+} assists in the progressive formation of the electrode–electrolyte interphase, providing the energetic dual-cation storage mechanisms.[20] We herein demonstrate the key role of NH_4^+ in regulating the hydroxylation degree of the derived high-mass-loading MnO_2, which is responsible for enhanced intrinsic capability of NH_4^+ storage (Scheme 1). More importantly, optimized MnO_2 dissolution chemistry is revealed with NH_4^+ in the electrode–electrolyte interface, leading to the collaborative dual-pathway energy storage. The reaction system and the new concept in the collaborative interface chemistry can help break the bottleneck toward energetic high-mass-loading energy storage (Scheme 1).

We start with the formation of an active MnO_2 substrate through phosphate-assisted *in situ* reconstruction.[20] By studying its charge/discharge properties in 0.5 M Mn^{2+} electrolyte, we found an increase of the CV curve area and thereby the areal capacitance value for the first 10 cycles (Fig. 1a and b), along with the increased active mass with cycling (SI Fig. 1). However, further cycling leads to a significant performance decline, indicating an unstable storage interface derived from poorly controlled deposition/dissolution chemistry. Increasing the Mn^{2+} concentration to 1 M leads to an increment of the areal capacitance, but the poor sustainability of the reaction system remains unsolved. In sharp contrast, we discovered that the areal capacitance exhibits a continuous increment during electrochemical cycling in the NH_4^+–Mn^{2+} mixed electrolyte, which achieves the highest value after 60 CV cycles (Fig. 1a and b). The derived 60-cycled electrode in NH_4^+–Mn^{2+} mixed electrolyte was denoted as Rec-NM-MnO_2 for further study.

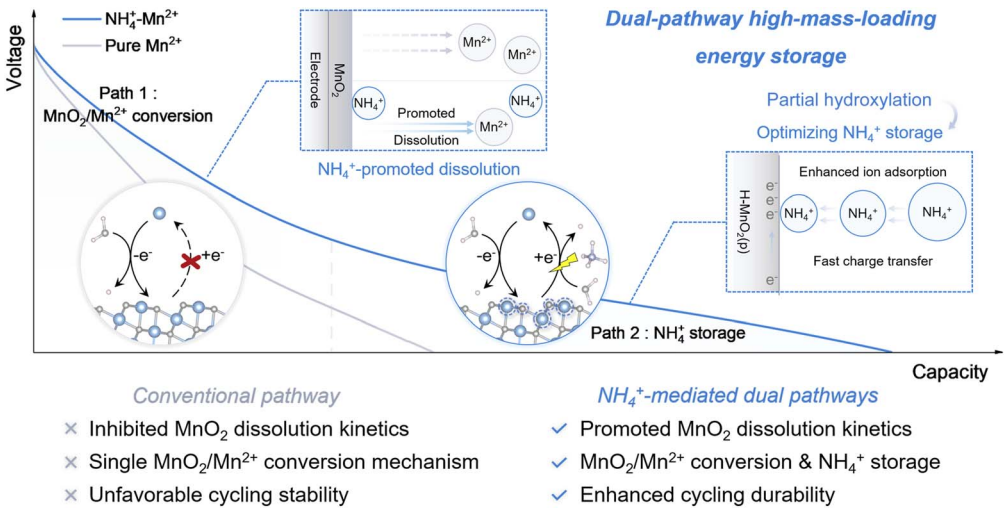

Scheme 1 Schematics of collaborative dual-pathway high-mass-loading energy storage.

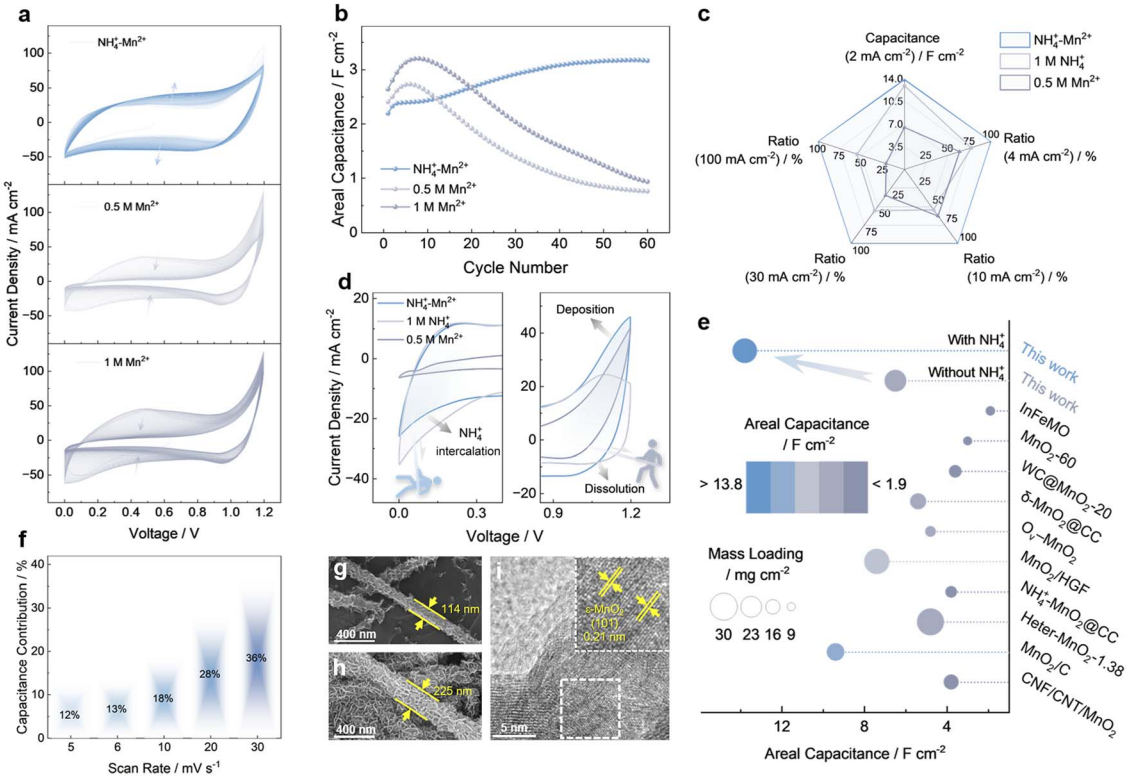

Fig. 1 Regulation of electrolytes and substrates. (a) CV curves of the activated MnO_2 substrate in different electrolytes. (b) Performance evolution of the active MnO_2 substrate with cycling in different electrolyte environments. (c) Comparison of areal capacitance for Rec-NM-MnO_2 in different electrolytes and the ratio of the capacitance measured in different electrolytes to that measured in NH_4^+–Mn^{2+} mixed electrolyte. (d) Comparison of CV curves at a scan rate of 2 mV s^{-1} for the Rec-NM-MnO_2 electrode in different electrolytes. (e) Comparison of the areal capacitance for the Rec-NM-MnO_2 electrode with previously reported high-mass-loading MnO_2-based electrodes. (f) Capacitive contributions for Rec-NM-MnO_2. (g and h) SEM images of Rec-NM-MnO_2 (g) before and (h) after electrochemical cycling. (i) HRTEM image of Rec-NM-MnO_2.

To further test the superiority of the mixed electrolyte system, we applied the bare carbon substrate (electrochemically exfoliated graphene, EG) to eliminate the influence of active MnO_2. A fast increase of areal capacitance with cycling was observed by using the pure EG substrate, ultimately achieving a decent areal capacitance of 9.3 F cm^{-2} at 2 mA cm^{-2} (SI Fig. 5). This result reflects the superiority of NH_4^+–Mn^{2+} mixed electrolyte to sustain the deposition/dissolution behaviors of MnO_2. Of note, a highly improved capacitance was demonstrated by applying the active MnO_2 electrode as the substrate (SI Fig. 5), attributed to more abundant nucleation sites and a larger accessible area for better deposition/dissolution chemistry. It delivers an appealing areal capacitance with a high value of 13.8 F cm^{-2} at 2 mA cm^{-2} and maintains an areal capacitance of 2.9 F cm^{-2} at 50 mA cm^{-2} (Fig. 1c and SI 3d), superior to many state-of-the-art high-mass-loading electrodes (Fig. 1e and SI Table S1).[6,21–29] Moreover, it displays good cycling stability with a retention of 80% after 6000 cycles (SI Fig. 3i).

The analysis of capacitive contribution and the *b* value by Dunn's method indicates a diffusion-controlled behavior during the charge-storage process (Fig. 1f and SI 2b). An asymmetric supercapacitor (Rec-NM-MnO_2//active carbon) was configured and investigated in the NH_4^+–Mn^{2+} mixed electrolyte. It delivers a high areal capacitance of 3.1 F cm^{-2} at 4 mA cm^{-2} (SI Fig. 6d), alongside a maximum energy density of 1070 μWh cm^{-2}, which is superior to many previously reported results (SI Fig. 6e).[30–36] Besides, it can operate stably for 500 cycles at a current density of 120 mA cm^{-2} (SI Fig. 6f). Please refer to SI Note 2 for details.

Revealing the reconstructed high-mass-loading electrode structure

To reveal the reconstructed structure, we first collected scanning electron microscopy (SEM) and high-resolution transmission electron microscopy (HRTEM) images. Before cycling, it demonstrates a core–shell heterostructure with ultra-thin nanosheets uniformly distributed (Fig. 1g and SI 7). It is noted that the unique structure with a large active area creates rich nucleation sites for the energetic MnO_2 deposition process, in good agreement with our electrochemical results (SI Fig. 5).[20] After 60 cycles in the NH_4^+–Mn^{2+} mixed electrolyte, the Rec-NM-MnO_2 microstructure features the dense stacking of nanosheets with an enlarged size and thickness compared to before, causing an increase of the overall diameter of the heterostructure from 114 nm to 225 nm and thereby an increment of mass loading from 7.4 mg cm^{-2} to 27.1 mg cm^{-2} (Fig. 1g, h, SI 7a and b and 8a–d). The accumulation of mass loading is further indicated by an increase of the charge transfer

resistance (R_{ct}) from 1.10 Ω to 6.12 Ω (SI Fig. 9a–c and Table S2). Notably, the system ohmic impedance (R_s) of the Rec-NM-MnO_2 electrode is as low as 0.61 Ω (SI Fig. 9a–c and Table S2), compared to the pristine electrode (0.49 Ω). Meanwhile, the Warburg factor (σ) of the samples after different cycles exhibits slight variation in the range of 3.6 to 5.55 (SI Fig. 9d), demonstrating a favorable ion diffusion capability in the thick electrode. The lattice spacing of 0.21 nm in HRTEM images can be indexed to the (101) plane of ε-MnO_2 (Fig. 1i and SI 8e).[37] One detail is the uniform distribution of N elements on the pristine active substrate, as shown by elemental mapping, which might come from intercalated NH_4^+ and the dopamine-derived N-doped carbon layer (SI Fig. 8f).

Ex situ X-ray diffraction (XRD) measurements were carried out to further reveal the structural evolution with cycling. As shown in Fig. 2a, the pristine active substrate shows diffraction peaks located at 36.2, 43.0, and 65.6°, indexed to the (110), (11-2), and (020) planes of δ-MnO_2 (JCPDS card no. 43-1456).[20,22,38] However, after cycling, the as-made Rec-NM-MnO_2 electrode exhibits diffraction peaks at 37.1, 42.4, and 66.2°, which are matched well with the (100), (101), and (110) planes of ε-MnO_2 (JCPDS card no. 30-0820), in good accordance with the HRTEM results.[39,40] The transformation of the main structure of the material is further reflected by the gradual shift of diffraction peaks with cycling (SI Fig. 10). Of note, there is an increase in the relative peak intensity of MnO_2 compared with that of the EG substrate, attributed to the gradual accumulation of ε-MnO_2 upon electrochemical cycling. These results indicate that, despite the enhanced kinetics, the active substrate features a higher deposition rate than that of the dissolution one during the early stage of cycling. The reconstructed reaction interface modulated by the accumulated ε-MnO_2 might play a key role in the highly improved electrochemical energy storage behaviors.

Ex situ X-ray photoelectron spectroscopy (XPS) measurement was conducted to study the evolution of the interfacial electronic structure. The peak separation energy (ΔE) of Mn 3 s increases from 4.91 eV for pristine MnO_2 to 5.13 eV after the first two cycles (Fig. 2b and SI 11a), suggesting the decrease of

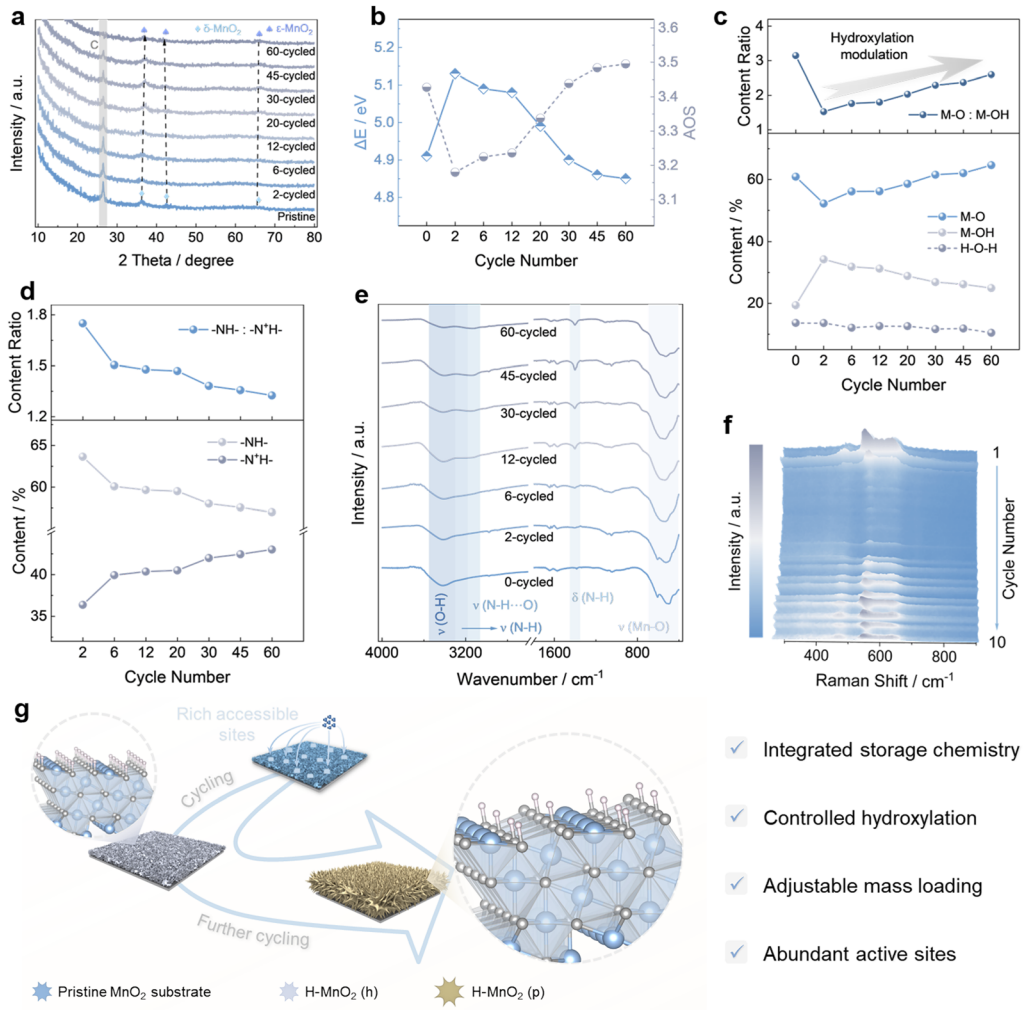

Fig. 2 Structure and composite analysis during electrochemical cycling. (a–e) *Ex situ* investigations of the active MnO_2 substrate: (a) XRD patterns; (b) ΔE value of Mn 3 s peaks and the AOS of Mn; characteristic content analysis based on (c) the O 1s spectra and (d) the N 1s spectra; (e) FTIR spectra. (f) *Operando* Raman contour maps of the active MnO_2 substrate during electrochemical cycling. (g) Schematic illustration of the development of the high-mass-loading partially hydroxylated ε-MnO_2 electrode.

the average oxidation state (AOS) of Mn from 3.42 to 3.18 with the accumulation of ε-MnO_2. Subsequently, the AOS of Mn increases to 3.49, demonstrating that surface oxidation happens with further cycling. This is also the case in the pure 0.5 M $Mn(NO_3)_2$ electrolyte (SI Fig. 12). The O 1s fine spectra can be decoupled and fitted into three components at 530.1, 531.6, and 533.2 eV, assigned to M–O–M, M–OH, and H–O–H, respectively (Fig. 2c and SI 11b).[41] The content ratio between M–O–M and M–OH bonds exhibits a reduction after the first two cycles and a gradual increase in the subsequent cycles. This suggests the initial formation of MnO_2 with a high hydroxylation degree (H-MnO_2(h)), but the hydroxylation degree shows a slight decrease with further cycling, yielding the partially hydroxylated MnO_2 (H-MnO_2(p)) for the Rec-NM-MnO_2 electrode. In the early stage, it is believed that a considerable amount of H^+ was produced with the hydrolysis of Mn^{2+} and the deprotonation effect of NH_4^+, which promotes the transformation from M–O–M to M–O–H bonds with discharging.[42] The similar evolution of M–O–M and M–O–H bonds is found during deposition in the pure 0.5 M Mn^{2+} electrolyte (SI Fig. 13). However, a relatively low hydroxylation degree was demonstrated, attributed to the inferior H^+ supply during hydroxylation.

The N 1s spectra of the pristine active substrate show two main peaks at 400.2 and 407.3 eV, attributed to the –NH– bond derived from dopamine (PDA)-derived carbon and NO_3^- from the $NaNO_3$ electrolyte, respectively (SI Fig. 11c).[20,43,44] Note that a new peak located at 401.4 eV, ascribed to the –N^+H– bond, appears at the second cycle, which originates from the NH_4^+ intercalated in MnO_2. Besides, the content ratio between –NH– and –N^+H– bonds gradually decreases with cycling (Fig. 2d and SI 11c), indicative of the varied main N source and the gradual accumulation of NH_4^+-intercalated MnO_2, which is also evidenced by XPS full-spectra (SI Fig. 11d and e). Moreover, it is also demonstrated by the *ex situ* Fourier transform infrared spectra (FTIR), where the characteristic absorptions indexed to the N–H bending vibration (1400 cm^{-1}), N–H···O bending vibration (3100–3180 cm^{-1}) and N–H stretching vibration (3180–3300 cm^{-1}) show an increase in intensity, while the peak indexed to the O–H stretching vibration (3300–3600 cm^{-1}) decays with cycling (Fig. 2e and SI 11f), which is consistent with the O 1s results (Fig. 2c).[23,45]

We focused on the first two cycles to study the structural evolution of the active substrate by *ex situ* characterization (SI Fig. 14–16). XRD results show periodic changes in the characteristic diffraction peaks (SI Fig. 14). There is a dynamic increase/decrease for the ratio of M–O–M/M–OH with reversible oxidation/reduction (SI Fig. 16), indicating H^+ participation in the early stage (please refer to SI Fig. 14–16 for details).

To gain more insights into the microstructure transformation, *operando* Raman characterization was performed. The pristine active substrate demonstrates three main peaks at 645 cm^{-1} (ν_1), 571 cm^{-1} (ν_2), and 497 cm^{-1} (ν_3), associated with the symmetric stretching vibration of the Mn–O bond along the d_{z^2} orbital within [MnO_6] octahedra, the stretching vibration in the basal plane along the $d_{x^2-y^2}$ orbital, as well as the weak Mn–O vibration mode, respectively (SI Fig. 17a).[46,47] The intensity of these major peaks (ν_1, ν_2, and ν_3) weakened during the first several cycles of deposition (Fig. 2f and SI 17b). This phenomenon might originate from the generation and accumulation of new substances, *i.e.*, hydroxylated MnO_2 on the surface of the original MnO_2 as discussed (Fig. 2c and SI 11b). As the hydroxylation degree slightly decreases with cycling, the characteristic peaks of MnO_2 demonstrate increasing intensity (Fig. 2f and SI 17b). We further focus on the *operando* Raman spectra during the 10th cycle with the well-defined characteristic peaks. As shown in Fig. 2f and SI 17d, with charging, ν_1 and ν_2 shift negatively and positively, respectively, and both of them shift back to the original locations upon discharging, indicating a highly reversible lattice deformation with NH_4^+ insertion/extraction.[8,23,47–52] A similar evolution trend was observed during the 1st cycle, except for the spectra in the potential range from 0 to 0.19 V. This unique oscillation phenomenon indicates a significant change in the surface chemical environment with the voltage applied (Fig. 2f and SI 17c).

XPS depth profiles were collected to gain more insights into the surface-accumulated hydroxylated ε-MnO_2 of the derived Rec-NM-MnO_2 electrode. A high content of Mn–OH (>20%) was found after different etching times, indicative of the considerable hydroxylation degree in the bulk structure upon cycling (Fig. 3f and SI 18b). It is further found that the outermost surface of the electrode demonstrates a higher hydroxylation degree.

The above results have evidenced the interface reconstruction with the accumulation of H-MnO_2(p) with high mass loading when cycling in the mixed NH_4^+–Mn^{2+} electrolyte (Fig. 2g), responsible for a significant increase in electrochemical performance (Fig. 1e and SI Table S1).

Understanding the role of NH_4^+ in the reconstructed interface

After understanding the promising nature of H-MnO_2(p), we further performed a series of electrochemical analyses and *in situ*/*ex situ* characterization experiments to gain insights into two questions: (1) what is the key role of NH_4^+ in boosting high-mass-loading energy storage? (2) How does NH_4^+ help overcome the inherent dissolution kinetics limitations?

We first studied the electrochemical behaviors of the Rec-NM-MnO_2 electrode in the pure 0.5 M $(NH_4)_2SO_4$ or 0.5 M $Mn(NO_3)_2$ electrolyte. The electrode exhibits a higher areal capacitance value in the mixed electrolyte than its counterparts, reinforcing an effective collaborative storage mechanism (Fig. 1c, SI 3a–d and 4). It displays a pronounced oxidation current by using the NH_4^+–Mn^{2+} or 0.5 M $Mn(NO_3)_2$ electrolyte (Fig. 1d and SI 3e), attributed to Mn^{2+}-to-MnO_2 deposition in the Mn^{2+} rich reaction environment.[53,54] In contrast, the reduction current from 1.2 V to 0.9 V increases a lot with NH_4^+ introduction (Fig. 1d and SI 3e), suggesting a unique role of NH_4^+ in promoting MnO_2 dissolution, which contributes to an increased discharge capacitance.[53,54]

This is also demonstrated by the charge evolution analysis of the Rec-NM-MnO_2 electrode (SI Fig. 3f and g), wherein an obvious charge accumulation was observed in the pure Mn^{2+} electrolyte, indicative of inadequate dissolution dynamics. In

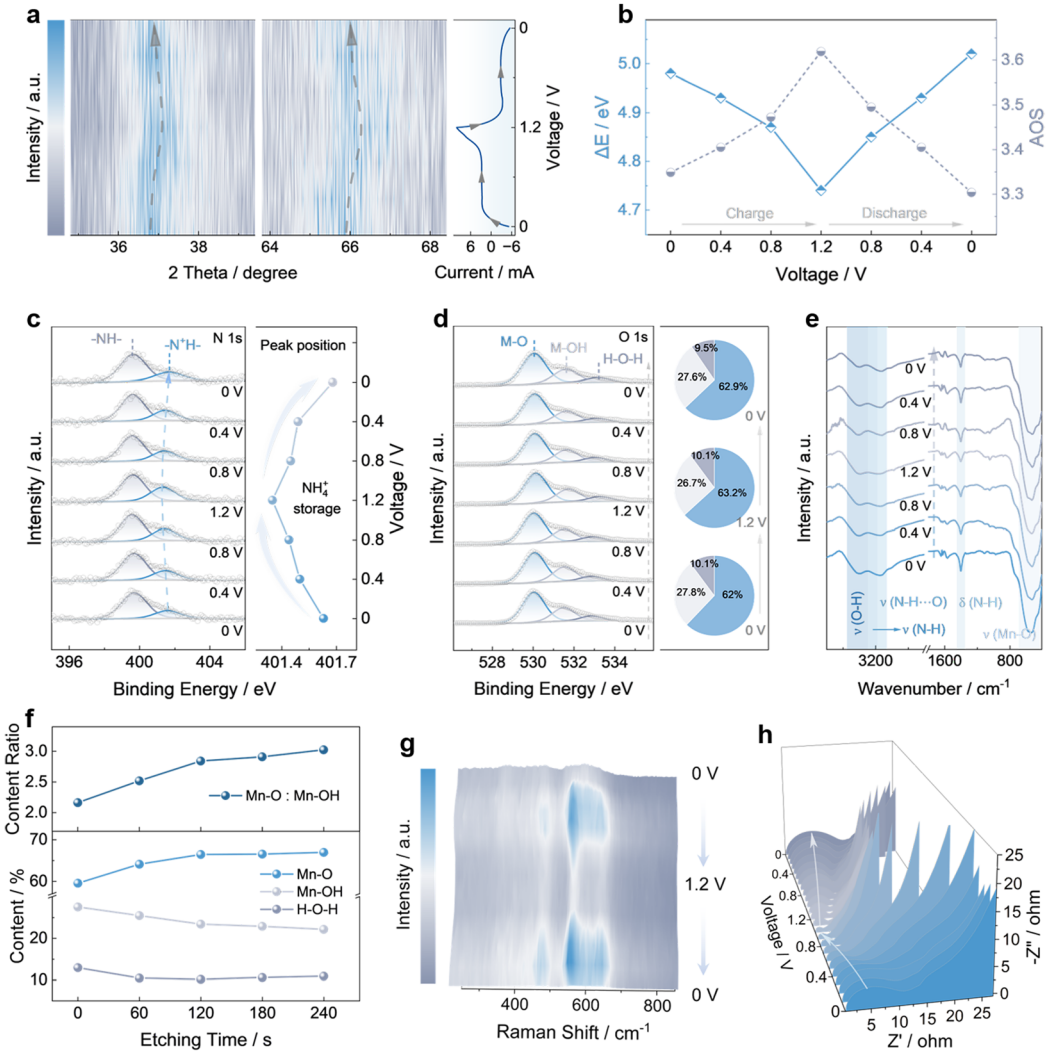

Fig. 3 Study of the energy storage mechanism of Rec-NM-MnO_2. (a–e) *Ex situ* characterization of the Rec-NM-MnO_2 electrode at different voltages: (a) XRD patterns; (b) Δ*E* value of Mn 3 s peaks and the AOS of Mn; (c) N 1s spectra and position variation of the peak relative to the –N^+H- bond; (d) O 1s spectra and corresponding content analysis; (e) FTIR spectra. (f) The content analysis of the O 1s spectra for Rec-NM-MnO_2 with different etching times. (g and h) *Operando* characterization of Rec-NM-MnO_2: (g) Raman contour map and (h) EIS spectra.

contrast, gradual charge consumption was found when cycling in the pure NH_4^+ electrolyte, implying promoted MnO_2 dissolution with NH_4^+ introduction. This is further evidenced by significantly weakened charge accumulation in NH_4^+–Mn^{2+} mixed electrolyte in comparison to that in the pure Mn^{2+} electrolyte.[55] In addition, with further discharging, an obvious reduction peak was observed in NH_4^+- Mn^{2+} or 0.5 M $(NH_4)_2SO_4$ electrolyte (Fig. 1d and SI 3e), which might originate from the extensive intercalation of NH_4^+ in the NH_4^+-rich environments.[23,54] We have further studied the electrochemical behaviors in a series of mixed electrolyte environments, evidencing the unique role of NH_4^+ in boosting charge-storage capability of the reaction system (SI Fig. 3h).

Then, we studied the energy storage mechanism of the Rec-NM-MnO_2 electrode in the NH_4^+–Mn^{2+} mixed electrolyte. According to *ex situ* XRD patterns, the diffraction peaks, relative to the (110) and (020) planes of ε-MnO_2, demonstrate a positive shift of 0.6° and 0.5° with charging, respectively, and return to the original locations upon discharging, which might originate from the interaction between NH_4^+ and ε-MnO_2 (Fig. 3a).[56] This is accompanied by the reversible change of the average oxidation state (AOS) of Mn (Fig. 3b and SI 18a). The characteristic peak indexed to the –NH^+- bond displays a negative shift of ~0.3 eV with charging (Fig. 3c), and shifts back upon discharging, implying the reversible deintercalation/intercalation of NH_4^+ and its potential interaction with MnO_2. Another detail is the negligible change of Mn–O–H content upon discharging, indicative of the negligible contribution of H^+ storage after interface reconstruction, which is responsible for the enhanced cycling stability (Fig. 3d).[57] This phenomenon is attributed to the accumulation of ε-MnO_2 with partial hydroxylation during cycling, which leads to the fast consumption of free H^+ in the electrolyte environment. Moreover, the FTIR spectra demonstrate the reversible decrease/increase of peak intensity for the N–H/N–H···O bending vibration and N–H stretching vibration during charging/discharging, while the peak indexed to the O–

H stretching vibration shows a negligible change, reinforcing that NH_4^+ serves as the charge carrier during the energy storage process (Fig. 3e and SI 18c).

We further collected the *operando* Raman spectra of the Rec-NM-MnO_2 electrode for tracking the NH_4^+ storage behaviors. With charging, ν_1 shifts positively from 639 cm^{-1} to 650 cm^{-1} (Fig. 3g and SI 19), ascribed to the oxidation of the Mn element and enhancement of the Mn–O stretching vibration along the d_{z^2} orbital of [MnO_6] octahedra due to the extraction of NH_4^+.[23,47–50] Moreover, the ν_2 peak shows an enhanced intensity and a negative shift of 8 cm^{-1} from 580 cm^{-1} to 572 cm^{-1} during charging, originating from the increase of Mn(IV) in the [MnO_6] framework and reduced Jahn–Teller disorder, accompanied by NH_4^+ deintercalation.[8,47,52] Both of them shift back to the pristine locations upon discharging, indicative of the reversible structural change with charge carrier deintercalation/intercalation. *Operando* electrochemical impedance spectra (EIS) of the Rec-NM-MnO_2 electrode demonstrate that the semicircle diameter indexed to the charge transfer resistance (R_{ct}) decreases with charging, while the slope in the low-frequency region relative to the ionic diffusion process increases (Fig. 3h and SI 2a). The reversed changes were observed with discharging, further confirming the highly reversible evolution of reaction dynamics.

The above results indicated that NH_4^+ serves as the charge carrier during the charge/discharge process of the Rec-NM-MnO_2 electrode. To further study the effect of NH_4^+ in the mixed reaction system, the electrochemical behaviors of Rec-NM-MnO_2 were further studied in the pure Mn^{2+} electrolyte. In this case, the capacitance gradually falls behind that in the NH_4^+–Mn^{2+} mixed electrolyte with cycling (Fig. 4a). *Ex situ* XPS results demonstrate the irreversible change of the AOS of Mn after one charge/discharge cycle in the pure Mn^{2+} electrolyte, resulting in a higher oxidation state of Mn (SI Fig. 20), indicative of an unsatisfactory dissolution dynamics. The fast MnO_2 accumulation but unfavorable dissolution kinetics, *i.e.*, an irreversible deposition/dissolution process, serve as the main cause of a fast discharge capacitance decay. The inconspicuous variation in

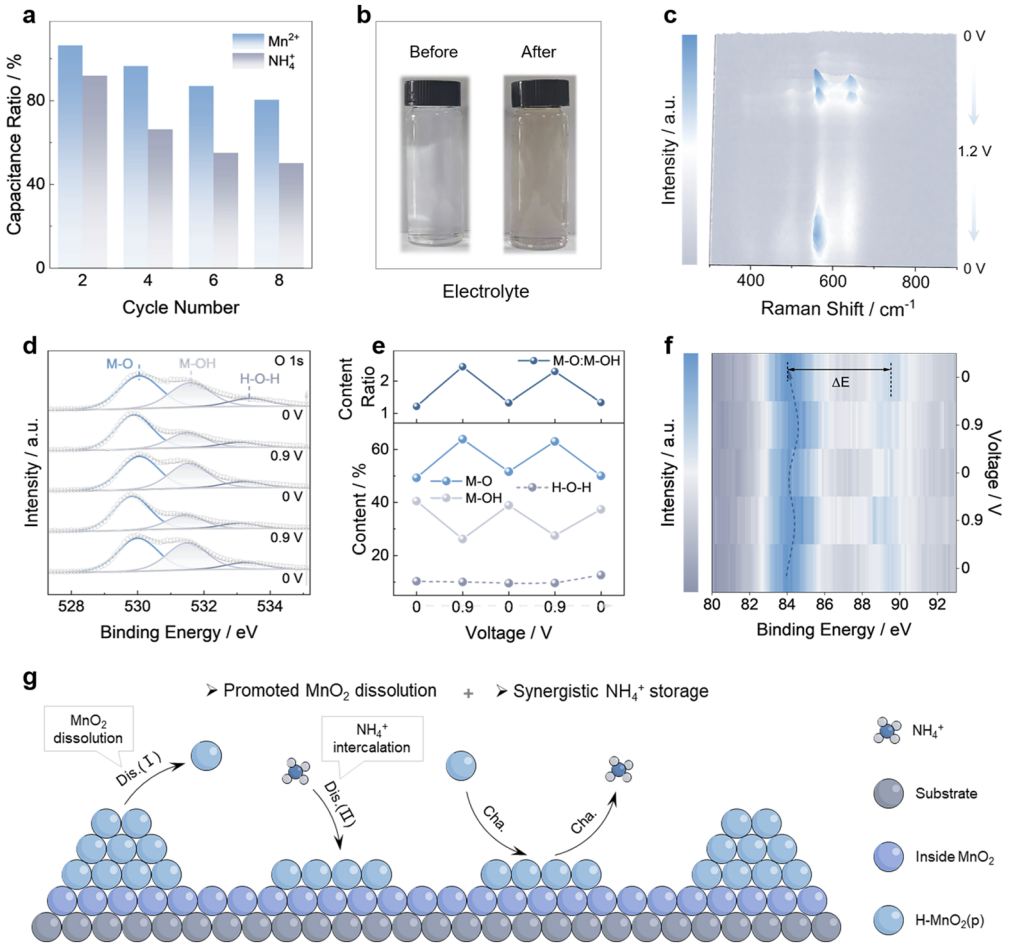

Fig. 4 Understanding the MnO_2 dissolution behavior assisted by NH_4^+. (a) The capacitance ratio of the Rec-NM-MnO_2 electrode in the 0.5 M $Mn(NO_3)_2$ or 0.5 M $(NH_4)_2SO_4$ electrolyte to that in the NH_4^+–Mn^{2+} mixed electrolyte at 2 mA cm^{-2}. (b) The digital images of $(NH_4)_2SO_4$ electrolyte before and after cycling. (c) *Operando* Raman contour map of Rec-NM-MnO_2 in 0.5 M $(NH_4)_2SO_4$ electrolyte. (d–f) *Ex situ* XPS characterization of the Rec-NM-MnO_2 electrode during the first two GCD cycles in the pure 0.5 M $(NH_4)_2SO_4$ electrolyte: (d) O 1s spectra; (e) content analysis of the O 1s spectra; (f) Mn 3 s spectra. (g) Schematic diagram of the electrochemical behavior for Rec-NM-MnO_2 in the NH_4^+–Mn^{2+} mixed electrolyte.

the content of the Mn–O–H bond also manifests the negligible contribution of H^+ storage in the pure Mn^{2+} electrolyte (SI Fig. 21).

Of particular note, the capacitance of Rec-NM-MnO_2 in the pure NH_4^+ electrolyte displays a dramatic decline, with only 52% of the capacitance retained compared with that in the mixed electrolyte after 8 cycles (Fig. 4a). At the same time, we noticed the significantly darkened brown color of the electrolyte (Fig. 4b). This detail indicates the fast dissolution of active Mn species into Mn ions, accompanied by the irreversible disproportionation of Mn^{3+} in the pure NH_4^+ electrolyte, which triggers the sharp decrease of capacitance. *Operando* Raman characterization was employed to further study the microstructure evolution after adopting the pure NH_4^+ electrolyte. ν_1 demonstrates a positive shift of 15 cm^{-1} during charging (Fig. 4c and SI 22), analogous to the scenario in the mixed electrolyte, suggesting the extraction of NH_4^+ and the oxidation of Mn centers.[23,47–50] Nevertheless, no reverse shift is observed for the ν_1 peak in the discharge stage (Fig. 4c and SI 22), indicating the emergence of irreversible oxidation/dissolution processes, in good accordance with our discussion, as shown in Fig. 4a. This is in good agreement with our electrochemical results in the pure NH_4^+ electrolyte, *e.g.*, the considerable increase of the reduction current (Fig. 1d), the variation of charge accumulation (SI Fig. 3f and g), and the decreased discharge capacitance (Fig. 4a), which concurrently evidence an NH_4^+-promoted dissolution dynamics.[58,59]

Through the *ex situ* XPS measurement, we noticed a considerable change in the content of the Mn–O–H bond during charging/discharging(Fig. 4d and e), indicating a significant proton-storage process along with local structural distortion, which destabilizes the structure and facilitates the dissolution of MnO_2 during electrochemical processes. Besides, the most significant variation range of the AOS of Mn (0.47) was found in the pure NH_4^+ electrolyte (Fig. 4f and SI 23a). The periodic shifts of the –N^+H– peak are associated with the intercalation and deintercalation of NH_4^+ during the cycles (SI Fig. 23b and c). The intercalated NH_4^+ could also increase local structural disorder, facilitating the interaction of MnO_2 with H^+ for enhanced dissolution kinetics.[47]

In addition, in the NH_4^+–Mn^{2+} mixed electrolyte system, NH_4^+ competes with Mn^{2+} for weakly bound water molecules in the outer solvation sheath through hydrogen bonds and ion–dipole interactions (with solvated H_2O), which breaks the compact and ordered solvation configuration of $[Mn(H_2O)_6]^{2+}$ in the pure Mn^{2+} electrolyte.[60,61] This reconstruction increases the diversity and weakens the aggregation of solvation structures, thereby elevating the solvation-configurational entropy.[62,63] It has been reported that high solvation-configurational entropy can effectively reduce the desolvation energy barrier and accelerate interfacial charge-transfer kinetics.[64,65] Meanwhile, the optimized solvation environment is expected to facilitate fast and reversible transport of both NH_4^+ and Mn^{2+} by reducing the desolvation energy barrier and weakening the electrostatic aggregation between cationic solvation clusters.[61,66] Additionally, the weakly aggregated solvation clusters can also suppress local ion concentration polarization and the subsequent severe interfacial side reactions, thus stabilizing the electrode/electrolyte interface and maintaining the structural integrity of partially hydroxylated MnO_2, contributing to good cycling stability.[67,68]

Therefore, with NH_4^+ introduced into the reconstructed reaction interface, a synergistic energy storage mechanism integrating the MnO_2 deposition/dissolution process coupled with NH_4^+ storage was enabled (Fig. 4g). This NH_4^+-assisted cationic environment not only overcomes the dissolution kinetics limitation but also brings additional capacitance contribution through NH_4^+ storage, leading to sustainable and collaborative dual-pathway high-mass-loading energy storage.

Deciphering the dual-pathway storage mechanism

The X-ray absorption near-edge structure (XANES) characterization was conducted to gain more insights into the evolution of active Mn species. In the Mn K-edge spectra, the absorption edge energy of Rec-NM-MnO_2 shows a positive shift to higher energy upon charging (Fig. 5a), indicating the increased oxidation state. Of particular note, the Mn species fabricated by 60 CV cycling in the pure Mn^{2+} system exhibits a higher valence at 0 V, which is even closer to that in the NH_4^+–Mn^{2+} mixed system at 1.2 V (Fig. 5a, SI 24a and b). This is mainly attributed to the sluggish dissolution dynamics for MnO_2 in the pure Mn^{2+} system, resulting in a higher oxidation state at the same discharged state, in good accordance with the *ex situ* XPS analysis. As shown in the Fourier-transformed (FT) k^3-weighted extended XAFS (FT-EXAFS) spectra in Fig. 5b, the peaks located at 1.42 and 2.43 Å indexed to Mn–O and Mn–Mn bonds, respectively, exhibit almost no change in shifts after charging to 1.2 V in NH_4^+–Mn^{2+} mixed electrolyte, implying the structural stability of Rec-NM-MnO_2 during cycling, in good accordance with the results of the *ex situ* O 1s spectra (Fig. 3d).[69,70] The wavelet transform (WT) analysis further corroborates that the intensity of the Mn–Mn bond experiences a slight increase as the operating voltage ascends (Fig. 5c). In the NH_4^+–Mn^{2+} mixed system, the slightly lower intensity of peaks at 0 V than that at 1.2 V is ascribed to insertion of NH_4^+ and the structural distortion derived from the decline of Mn valence (SI Fig. 24c). Furthermore, the R-space curve in the pure Mn^{2+} electrolyte shows a high similarity to that in NH_4^+–Mn^{2+} mixed electrolyte (SI Fig. 24d), demonstrating the same coordination environment of MnO_2 generated, consistent with the XRD analysis (SI Fig. 14c).

Our study has demonstrated the formation of partially hydroxylated MnO_2 (H-MnO_2(p)) as the true active species in the NH_4^+–Mn^{2+} mixed system to guide the deposition/dissolution process. For further clarification of the working mechanisms, density functional theory (DFT) simulations were conducted to study the influence of the hydroxylation degree on the interfacial reaction dynamics. As shown in SI Fig. 25, we chose pure ε-MnO_2 (named pure MnO_2), H-MnO_2(p), and H-MnO_2(h) (highly hydroxylated MnO_2) as models for the calculations. The H-MnO_2(p) and H-MnO_2(h) structures are modelled as ε-MnO_2 with small and large amounts of hydroxyl groups adsorbed on the (101) plane, respectively, according to our aforementioned experimental results. The density of states (DOS) calculation

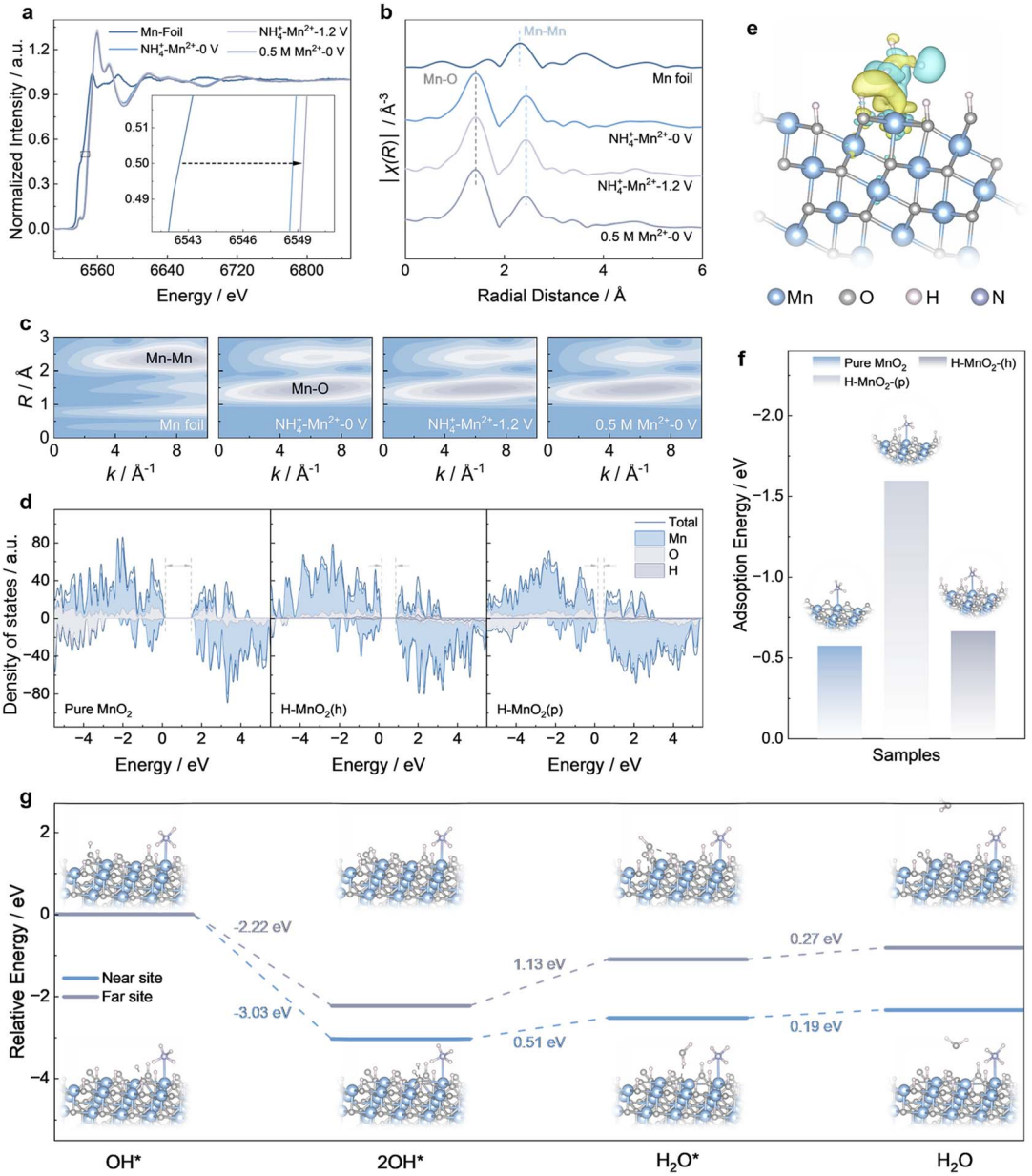

Fig. 5 Fine structure characterization and theoretical calculations for understanding the integrated storage mechanism. (a) Mn K-edge XANES spectra of the Rec-NM-MnO_2 electrode in NH_4^+–Mn^{2+} mixed electrolyte and the counterpart electrode derived in pure 0.5 M $Mn(NO_3)_2$ electrolyte at different states. (b) The k^3-weighted Fourier transformation of the Mn K-edge EXAFS spectra. (c) Wavelet transformation of the k^3-weighted Mn K-edge EXAFS signals. (d) Density of states for pure MnO_2, H-MnO_2(h), and H-MnO_2(p). (e) Differential charge density of NH_4^+ adsorbed on H-MnO_2(p) (the cyan and yellow colors correspond to charge depletion and accumulation, respectively). (f) Adsorption energies of NH_4^+ on the surface of pure MnO_2, H-MnO_2(h), and H-MnO_2(p). (g) Relative energy profile of the dissolution processes for the sites near (below) and far (above) from the adsorbed NH_4^+.

results demonstrate that the band gap decreases in the following sequence: pure MnO_2 > H-MnO_2(h) > H-MnO_2(p) (Fig. 5d), indicating the enhanced electron transfer capability of H-MnO_2(p).

To gain more information on the superiority of the storage capacitance of H-MnO_2(p) in the NH_4^+–Mn^{2+} mixed system, the charge density difference (CDD) analysis and adsorption energy for NH_4^+ on pure MnO_2, H-MnO_2(h), and H-MnO_2(p) were studied. As depicted in Fig. 5e, at an isosurface level of 0.002 e $Å^{-3}$, a pronounced charge-transfer behavior appears from the NH_4^+ side to the MnO_2 side, implying an intimate interfacial electronic interaction between NH_4^+ and H-MnO_2(p). In addition, the calculated NH_4^+ adsorption energy of H-MnO_2(p) was considerably lower than that of pure MnO_2 and H-MnO_2(h) (Fig. 5f), suggesting its kinetically favorable NH_4^+ adsorption stemming from the tailored interface microenvironment. We further calculated the Gibbs free energy to identify the synergistic modulation mechanism of NH_4^+ ions during the MnO_2

discharge process. As demonstrated in Fig. 5g, this process begins with a proton binding to a lattice oxygen atom on the MnO_2 surface, followed by an attack from a second proton. Remarkably, the second proton attack is more favorable at the nearby site, with an energy of −3.03 eV compared to −2.22 eV at the distal site (Fig. 5g). This is followed by the *in situ* formation of a structural H_2O molecule, which is a nonspontaneous process serving as the rate-determining step (RDS). Of note, the energy barrier for this RDS is markedly lower at the NH_4^+-proximal site (0.51 eV) compared to the distal site (1.13 eV), underscoring the critical role of NH_4^+ in promoting dissolution kinetics. Also, the proximal site demonstrates a low energy barrier for H_2O molecule release from the MnO_2 surface, signifying the facilitated dissolution behavior along with the interfacial proton/electron transfer.

Conclusions

In summary, we discovered NH_4^+-mediated interface chemistry for dynamically reshaping the hydroxylation degree of MnO_2 toward an optimal reconstructed interface, which ensures fast Mn^{2+}/MnO_2 conversion chemistry, and at the same time, creates a kinetically favorable microenvironment for efficient NH_4^+ storage. The as-enabled dual-pathway storage mechanism triggers a superior areal capacitance of 13.8 F cm^{-2} and good cycling stability at a superhigh mass loading of 27.1 mg cm^{-2}. Theoretical calculations indicate that local partial hydroxyl groups help strengthen the electronic conduction and facilitate the interfacial adsorption for NH_4^+ storage. The adsorbed NH_4^+ triggers the redistribution of local electrons and thereby results in a considerably reduced uphill energy barrier of the non-spontaneous rate-determining step of the dissolution process, enabling a collaborative dual-pathway storage behavior. This research establishes a study paradigm focusing on the synergistic dual-pathway mechanism by refining the interfacial microenvironment for better high-mass-loading energy storage.

Author contributions

W. G. and Q. Z. supervised the research. J. W. and W. G. designed the experimental routes. J. W. carried out the material fabrication and most of the characterization experiments. J. W. and W. G. conducted the main data analysis and the paper writing. J. W., M. S., N. H., and Y. Y. carried out electrochemical measurements. J. W., W. G., G. Z., M. C., and W. X. performed *operando* Raman characterization. All co-authors contributed to discussions on the relative results and improving the paper.

Conflicts of interest

There are no conflicts to declare.

Data availability

The data supporting this article have been included as part of the supplementary information (SI). Supplementary information: the detailed experimental procedures for electrode fabrication, materials characterization, electrochemical measurements, and density functional theory (DFT) computational methods, mass variation data, charge storage dynamics analysis, electrochemical performance comparisons across different electrolytes and substrates, characterization of asymmetric supercapacitors, scanning and transmission electron microscopy images, *operando* electrochemical impedance spectroscopy, *ex situ* X-ray diffraction patterns, X-ray photoelectron spectra, Fourier-transform infrared spectra, *operando* Raman spectra, X-ray absorption near-edge structure data, additional interpretive analysis, performance comparisons with literature reports, and fitted equivalent circuit parameters from impedance measurements. See DOI: https://doi.org/10.1039/d6sc02038k.

Acknowledgements

The authors thank the National Natural Science Foundation of China (Grant No. 51673156 for Q. Z., 52202301 for W. G., and 22375161 for W. G.), China Postdoctoral Science Foundation (2022TQ0256 for W. G. and 2022M722587 for W. G.), and Innovation Foundation for Doctor Dissertation of Northwestern Polytechnical University (CX2024093 and CX2025094) for their great support. We also thank eceshi (https://www.eceshi.com) for the theoretical calculations and the Anhui Absorption Spectroscopy Analysis Instrument Co, Ltd for XAFS measurements and analysis.

References

1 A. Noori, M. F. El-Kady, M. S. Rahmanifar, R. B. Kaner and M. F. Mousavi, *Chem. Soc. Rev.*, 2019, **48**, 1272–1341.
2 P. Simon and Y. Gogotsi, *Nat. Mater.*, 2008, **7**, 845–854.
3 P. Simon and Y. Gogotsi, *Nat. Mater.*, 2020, **19**, 1151–1163.
4 J. Peng, W. Zhang, S. Wang, Y. Huang, J. Z. Wang, H. K. Liu, S. X. Dou and S. L. Chou, *Adv. Funct. Mater.*, 2022, **32**, 2111720.
5 X. S. Cui, Q. F. Wu, S. Y. Wang, J. Z. Wang, W. L. Qubie, Y. X. Zhang, J. L. Zhang and J. C. Fu, *Small*, 2025, **21**, e05422.
6 Z. Y. Peng, Y. T. Huang, A. G. Bannov, S. L. Li, L. Tang, L. C. Tan and Y. W. Chen, *Energy Environ. Sci.*, 2024, **17**, 3384–3395.
7 J. Ma, C. Li, Q. Q. Ji, C. L. Liu, B. Tang, R. Q. Liu, Y. Y. Liu, N. Li, C. Wang, J. R. Zeng, K. Zheng and W. S. Yan, *Angew. Chem., Int. Ed.*, 2025, **64**, e202513148.
8 W. Guo, C. Dun, F. P. Yang, C. Zhan, J. J. Urban, J. H. Guo and Q. Y. Zhang, *ACS Nano*, 2023, **17**, 25357–25367.
9 Y. J. Zhao, S. X. Zhang, Y. Y. Zhang, J. R. Liang, L. T. Ren, H. J. Fan, W. Liu and X. M. Sun, *Energy Environ. Sci.*, 2024, **17**, 1279–1290.
10 G. J. Lai, X. T. Hu, S. B. Liang, Y. Q. Yang, E. R. Elsharkawy, G. A. M. Mersal, B. A. Lu, Z. M. El-Bahy, Y. Y. Liu and J. Zhou, *ACS Energy Lett.*, 2025, **10**, 3437–3444.
11 T. Zhang, T. Li, Y. Shen, H. X. Ma, C. Y. Wei, J. H. Cai, Y. Xu, Y. Y. Li, X. J. Dong, S. C. Zhang, F. Q. Huang and T. Q. Lin, *Adv. Mater.*, 2025, **37**, 2505082.

12 W. Guo, C. Yu, C. T. Zhao, Z. Wang, S. F. Li, J. H. Yu, X. Y. Tan, Y. Y. Xie, L. Yang, H. L. Huang, R. Fu and J. S. Qiu, *Energy Storage Mater.*, 2020, **31**, 172–180.
13 X. M. Han, R. Zhao, L. Y. Yu, L. H. Wang, X. Y. Zhang, A. Q. Zhang, J. J. Yang, Z. F. Hu, M. G. Lv, T. X. Miao, F. Wu, Y. Bai and C. Wu, *Adv. Mater.*, 2025, **31**, e13548.
14 J. Feng, X. Y. Li, Y. X. Ouyang, H. Y. Zhao, N. Li, K. Xi, J. Y. Liang and S. J. Ding, *Angew. Chem., Int. Ed.*, 2024, **63**, e202407194.
15 C. X. Li, W. Guo, J. X. Wang, W. B. Dang and Q. Y. Zhang, *Angew. Chem., Int. Ed.*, 2025, **64**, e202422403.
16 W. Guo, F. P. Yang, C. Yu, Y. Y. Xie, J. K. Chen, Y. S. Liu, Y. Zhao, J. Yang, X. F. Feng, S. F. Li, Z. Wang, J. H. Yu, K. L. Liu, K. Qian, M. Tsige, Q. Y. Zhang, J. H. Guo and J. S. Qiu, *Matter*, 2021, **4**, 2902–2918.
17 W. Guo, C. Yu, S. F. Li and J. S. Qiu, *Energy Environ. Sci.*, 2021, **14**, 576–601.
18 Y. X. Wen, Y. P. Liu, T. Wang, Z. L. Wang, Y. A. Zhang, X. G. Wu, X. T. Chen, S. L. Peng and D. Y. He, *ACS Appl. Energy Mater.*, 2021, **4**, 6531–6541.
19 D. Geng, S. Zhang, Y. T. Jiang, Z. M. Jiang, M. J. Shi, J. Chang, S. C. Liang, M. Y. Zhang, J. Feng, T. Wei and Z. J. Fan, *J. Mater. Chem. A*, 2022, **10**, 2027–2034.
20 J. X. Wang, W. Guo, M. M. Sun, G. Zhang, Y. Meng and Q. Y. Zhang, *Energy Environ. Sci.*, 2025, **18**, 960–971.
21 J. M. Jeong, S. H. Park, H. J. Park, S. B. Jin, S. G. Son, J. M. Moon, H. Suh and B. G. Choi, *Adv. Funct. Mater.*, 2021, **31**, 2009632.
22 J. X. Wang, W. Guo, Z. X. Liu and Q. Y. Zhang, *Adv. Energy Mater.*, 2023, **13**, 2300224.
23 Q. Chen, J. L. Jin, M. D. Song, X. Y. Zhang, H. Li, J. L. Zhang, G. Y. Hou, Y. P. Tang, L. Q. Mai and L. Zhou, *Adv. Mater.*, 2022, **34**, 2107992.
24 S. F. Zhang, L. Li, Y. L. Liu and Q. L. Li, *Carbohydr. Polym.*, 2024, **326**, 121661.
25 Q. H. Cao, J. J. Du, X. W. Tang, X. Xu, L. S. Huang, D. M. Cai, X. Long, X. W. Wang, J. Ding, C. Guan and W. Huang, *Research*, 2020, 7304767.
26 H. Y. Quan, Z. K. Tu, Z. H. Fang, B. Q. Tan, X. Wang and D. Z. Chen, *J. Energy Storage*, 2025, **133**, 118001.
27 L. Chen, F. Wang, Z. W. Tian, H. T. Guo, C. Y. Cai, Q. J. Wu, H. J. Du, K. M. Liu, Z. F. Hao, S. J. He, G. G. Duan and S. H. Jiang, *Small*, 2022, **18**, 2201307.
28 Z. H. Huang, Y. Song, D. Y. Feng, Z. Sun, X. Q. Sun and X. X. Liu, *ACS Nano*, 2018, **12**, 3557–3567.
29 B. R. Li, Y. F. Chu, B. Xie, Y. C. Sun, L. Zhang, H. M. Zhao, L. Zhao, P. F. Liu and J. J. He, *J. Mater. Chem. A*, 2023, **11**, 2133–2144.
30 F. Y. Xie, Y. Du, M. H. Chu, X. Y. Jia, H. Cao, R. Zhang, H. W. Li and M. Zhang, *Chem. Eng. J.*, 2025, **513**, 162864.
31 Y. J. Lei, W. L. Zhao, Y. P. Zhu, U. Buttner, X. C. Dong and H. N. Alshareef, *ACS Nano*, 2022, **16**, 1974–1985.
32 B. Shi, L. Li, A. B. Chen, T. C. Jen, X. Y. Liu and G. Z. Shen, *Nano-Micro Lett.*, 2022, **14**, 34.
33 L. Naderi and S. Shahrokhian, *Nanoscale*, 2022, **14**, 9150–9168.
34 Z. Y. Han, X. Y. Zhang, G. L. Tang, J. Liang and W. Wu, *J. Energy Storage*, 2024, **91**, 112023.
35 D. D. Ling, D. H. Zhang and Q. F. Wang, *Chem. Eng. J.*, 2025, **520**, 166064.
36 S. J. Xiong, X. X. Li, G. S. Li, Z. L. Wang, Z. J. Wang, M. D. Guo, C. K. Zhang, Y. N. Ma and T. C. Zeng, *Adv. Funct. Mater.*, 2025, **36**, e13738.
37 J. Z. Yang, S. S. Bi, H. M. Wang, Y. Y. Zhang, H. X. Yan and Z. Q. Niu, *Angew. Chem., Int. Ed.*, 2024, **63**, e202409071.
38 X. H. Zhu, J. Xu, Q. H. Zhang, T. Shen, Y. H. Zhuang, T. T. Chen, S. Li, L. Gu and H. Xia, *Nat. Commun.*, 2025, **16**, 3838.
39 H. Y. Chen, P. C. Ruan, H. Zhang, Z. M. El-Bahy, M. M. Ibrahim, B. G. Lu and J. Zhou, *Angew. Chem., Int. Ed.*, 2025, **64**, e202423999.
40 W. J. Fan, S. Y. Tian, L. P. Qin, T. S. Alomar, P. C. Ruan, Z. M. El-Bahy, N. AlMasoud, B. G. Lu and J. Zhou, *J. Am. Chem. Soc.*, 2025, **147**, 18694–18703.
41 W. L. Zhao, F. H. Xu, L. Q. Liu, M. Liu and B. C. Weng, *Adv. Mater.*, 2023, **35**, 2308060.
42 M. X. Li, C. Liu, J. M. Meng, P. Hei, Y. Sai, W. J. Li, J. Wang, W. B. Cui, Y. Song and X. X. Liu, *Adv. Funct. Mater.*, 2024, **34**, 2405659.
43 Y. H. Gao, T. Song, X. L. Guo, Y. Zhang and Y. Yang, *Green Carbon*, 2023, **1**, 105–117.
44 W. Q. Wei, Z. Wei, R. Z. Li, H. Yuan, J. S. Chen, J. Lv and S. X. Ouyang, *Green Carbon*, 2024, **2**, 291–299.
45 Y. Song, Q. Pan, H. Z. Lv, D. Yang, Z. M. Qin, M. Y. Zhang, X. Q. Sun and X. X. Liu, *Angew. Chem., Int. Ed.*, 2021, **60**, 5718–5722.
46 Q. N. Zhang, M. D. Levi, Q. Y. Dou, Y. L. Lu, Y. G. Chai, S. L. Lei, H. X. Ji, B. Liu, X. D. Bu, P. J. Ma and X. B. Yan, *Adv. Energy Mater.*, 2019, **9**, 1802707.
47 D. C. Chen, D. Ding, X. X. Li, G. H. Waller, X. H. Xiong, M. A. El-Sayed and M. L. Liu, *Chem. Mater.*, 2015, **27**, 6608–6619.
48 Y. K. Hsu, Y. C. Chen, Y. G. Lin, L. C. Chen and K. H. Chen, *Chem. Commun.*, 2011, **47**, 1252–1254.
49 L. Y. Liu, L. J. Su, Y. L. Lu, Q. N. Zhang, L. Zhang, S. L. Lei, S. Q. Shi, M. D. Levi and X. B. Yan, *Adv. Funct. Mater.*, 2019, **29**, 1806778.
50 T. Xiao, C. Tang, H. X. Lin, X. R. Li, Y. T. Mei, C. Xu, L. Gao, L. H. Jiang, P. Xiang, S. B. Ni, Y. Q. Xiao and X. Y. Tan, *Inorg. Chem.*, 2024, **63**, 17714–17726.
51 L. F. Yang, S. Cheng, X. Ji, Y. Jiang, J. Zhou and M. L. Liu, *J. Mater. Chem. A*, 2015, **3**, 7338–7344.
52 L. F. Yang, S. Cheng, J. H. Wang, X. Ji, Y. Jiang, M. H. Yao, P. Wu, M. K. Wang, J. Zhou and M. L. Liu, *Nano Energy*, 2016, **30**, 293–302.
53 X. L. Ye, D. L. Han, G. Y. Jiang, C. J. Cui, Y. Guo, Y. G. Wang, Z. C. Zhang, Z. Weng and Q. H. Yang, *Energy Environ. Sci.*, 2023, **16**, 1016–1023.
54 Y. Q. Wang, H. Hong, Z. Q. Wei, D. D. Li, X. R. Yang, J. X. Zhu, P. Li, S. N. Wang and C. Y. Zhi, *Energy Environ. Sci.*, 2025, **18**, 1524–1532.
55 J. F. Lei, Y. X. Yao, Z. Y. Wang and Y. C. Lu, *Energy Environ. Sci.*, 2021, **14**, 4418–4426.

56 Z. Z. Liu, W. H. Zhou, J. He, H. Chen, R. X. Zhang, Q. Wang, Y. Wang, Y. G. Yan and Y. G. Chen, *J. Alloys Compd.*, 2021, **869**, 159279.
57 X. L. Li, Z. B. Xu, Y. T. Qian and Z. G. Hou, *Energy Storage Mater.*, 2022, **53**, 72–78.
58 X. Z. Xue, Z. Liu, S. Chandrasekaran, S. Eisenberg, C. Althaus, M. C. Freyman, A. Pinongcos, Q. Ren, L. Valdovinos, C. T. Hsieh, B. T. Hu, B. Dunn, C. A. Orme, X. Wang, M. A. Worsley and Y. T. Li, *Adv. Mater.*, 2025, **37**, 2419505.
59 J. Cui, Z. K. Liu, C. Q. Song, Z. D. Meng and P. Kang, *Small*, 2025, **21**, 2506034.
60 C. Yi, L. Jiao, Y. S. Fu, C. Wang, Z. Q. Ruan, J. J. Liu, X. S. Yang, S. S. Yu, Y. C. Lei, T. Zhang, L. X. Yang, D. K. Shu, S. Yang, C. Y. Li, H. Li, W. J. Zhang and B. W. Cheng, *Adv. Energy Mater.*, 2026, **16**, e04881.
61 J. T. Yu, X. Y. Ma, X. Y. Zou, Y. Hu, M. C. Yang, Y. L. Cai and F. Yan, *Angew. Chem., Int. Ed.*, 2025, **64**, e202416092.
62 B. Liu, G. M. Yao, W. M. Gao, R. X. Wang, J. Xu, C. C. Yuan, B. J. Yang, Q. J. Fu, Y. X. Song, G. M. Zhou and X. J. Wei, *J. Am. Chem. Soc.*, 2026, **148**, 7663–7676.
63 F. Ai and Y. C. Lu, *Nat. Rev. Mater.*, 2025, **10**, 929–946.
64 W. D. Luo, H. W. Fu, P. Peng, C. T. Gao, M. Y. Gu, A. M. Rao, Z. Q. Dai, S. Q. Gu, J. Zhou, F. F. Sun, Y. M. He and B. A. Lu, *Joule*, 2026, **10**, 102271.
65 J. W. Huang, X. G. An, Z. L. Cheng, J. L. Jiang, Y. Bai, H. K. Liu, J. Peng, M. H. Wu, S. X. Dou, X. L. Sun and C. Wu, *J. Am. Chem. Soc.*, 2025, **147**, 46594–46607.
66 Z. Y. Ou, W. F. Zhang, Y. X. Gang, W. W. Zou, T. M. Ma, Y. F. Su, G. X. Jiang, X. Z. Zhang and L. Du, *Adv. Funct. Mater.*, 2026, DOI: 10.1002/adfm.202531692.
67 H. Yan, C. G. Hou, Y. M. Wang, Y. C. Guo, Y. M. Bai, H. Fu, X. Q. Li, W. J. Zhang, J. M. Kim and G. C. Liu, *Adv. Funct. Mater.*, 2026, DOI: 10.1002/adfm.202530600.
68 Y. H. Zhang, J. N. Liu, B. Y. Sun, S. J. Chen, Y. F. Hong, C. T. Lin, J. K. Deng and J. X. Song, *Angew. Chem., Int. Ed.*, 2026, **65**, e24476.
69 D. R. Wu, L. M. Housel, S. T. King, Z. R. Mansley, N. Sadique, Y. M. Zhu, L. Ma, S. N. Ehrlich, H. Zhong, E. S. Takeuchi, A. C. Marschilok, D. C. Bock, L. Wang and K. J. Takeuchi, *J. Am. Chem. Soc.*, 2022, **144**, 23405–23420.
70 S. Y. Yao, S. Y. Wang, R. C. Liu, X. Liu, Z. Z. Fu, D. W. Wang, H. G. Hao, Z. Y. Yang and Y. M. Yan, *Nano Energy*, 2022, **99**, 107391.